A graphene-based electrochemical device with thermoresponsive microneedles for diabetes monitoring and therapy

Hyunjae Lee[1,2,⊥], Tae Kyu Choi[1,2,⊥], Young Bum Lee[1,2,⊥], Hye Rim Cho[1,3], Roozbeh Ghaffari[4], Liu Wang[5], Hyung Jin Choi[6], Taek Dong Chung[7,8], Nanshu Lu[5], Taeghwan Hyeon[1,2], Seung Hong Choi[1,3], and Dae-Hyeong Kim[1,2]*

[⊥]These authors contributed equally to this work.

*To whom correspondence should be addressed.
E-mail: dkim98@snu.ac.kr

This supplementary information contains:
Supplementary Text, References, and Supplementary Figures

1. Supplementary Text

1.1. Electrode characterization using cyclic voltammograms and AC impedance measurements.

The electrochemical characterization of the Au film, Au mesh, and graphene-hybrid electrode in PBS with 10 mM $Fe(CN)_6^{3-/4-}$ are summarized in Supplementary Table 1. In cyclic voltammograms, the Au mesh shows peak currents at the higher potential than the others, suggesting that it has much higher charge transfer resistance (R_{ct}) for the redox reaction than the others, which is in good agreement with its Nyquist plot data (Fig. 2b,c). Under the same condition, the undoped CVD graphene film with and without Au mesh are electrochemically characterized. But it shows negligible amount of redox reactions and very high impedance values due to poor electrochemical activity of the CVD graphene (Supplementary Fig. 6a–c). On the other hand, the graphene-hybrid electrode shows lower R_{ct} and higher charge storage capacity (CSC) than other electrodes (Fig. 2b,c) due to the increase of electrochemically active surface area by the Au doping with the high thermal and cyclic stability (Supplementary Fig. 5c,d).

Electrochemically active surface areas of electrodes are estimated by using the Randles-Sevcik equation[1] and the well-known diffusion coefficient of ferri- and ferro-cyanide ions in aqueous media[2]. The graphene-hybrid electrode has a larger electrochemically active surface area than other electrodes (i.e., Au mesh and Au film; see Supplementary Table 1). We also calculated the electrochemically active surface area of other 2D[3] and 3D[4,5] graphene electrodes reported in the previous literatures. The results show that the graphene-hybrid electrode has a larger electrochemically active surface area than that of the 2D graphene electrode (calculated value: 0.080), but smaller than those of 3D graphene electrodes (calculated value: 2.189, 4.988). Although 3D graphene electrodes have large surface areas, they are not compatible with several fabrication processes, such as photolithography and transfer printing processes. In addition, they can be irreversibly deformed during wearable device applications, which can cause changes in electrochemical performances of devices. Therefore, our 2D graphene-hybrid electrode is chosen in the current integrated system.

Table 1. CV and AC impedance measurement data and estimated surface area for electrodes

Electrode	R_{ohm} (Ω cm^{-2})	R_{ct} (Ω cm^{-2})	C_{dl} (μF cm^{-2})	CSC (mC cm^{-2})	Normalized Area*
Au film	28	16	21.4534	1.005	0.797
Au mesh	23	490	0.8532	0.252	0.295
Graphene-hybrid	21	15	15.5291	1.307	1.135

* Normalized Area = Effective Electrochemically Active Surface Area / Geometric Surface Area

1.2. Mechanical analysis of electrodes.

Finite element modeling (FEM) of the mechanical robustness of the graphene-hybrid electrode is performed using ABAQUS/Standard 6.13. The exploded and cross-sectional views of the multilayer device are illustrated in Supplementary Fig. 8b. Au mesh and graphene sandwiched by epoxy in graphene-hybrid electrode, and Au or ITO film sandwiched by epoxy in conventional electrodes are both modeled as homogeneous shell (mesh element S4R) with different elastic properties. The Young's modulus, Poisson's ratio, and thickness of each layer used in our model are summarized in Supplementary Table 2.

Table 2. Mechanical properties values of different layers[6-10]

Materials	Young's modulus (GPa)	Poisson's ratio	Thickness (nm)
Epoxy	4.02	0.33	1500
Au	79	0.4	70
ITO	116	0.35	150
Graphene	1020	0.15	2
Cr/Au	97	0.39	77

The effective Young's modulus and Poisson's ratio of the Au mesh are calculated by weighing each component's volume fraction[11]. For the graphene-hybrid electrode, we first model an island composed of four blanket layers: epoxy, graphene, Au mesh, epoxy. The effective Young's modulus and Poisson's ratio of the graphene-hybrid electrode is found to be:

$$E_e = 5.0 \, GPa, v_e = 0.34.$$

In the following stretching and compression simulation, we model the island and serpentine as a homogeneous shell structure (element type S3) with Young's modulus E_e, Poisson's ratio v_e, and thickness 3079 nm. The substrate (a 0.2 mm thick slab of 1:40 PDMS) is modeled as a 3D Neo Hookean solid (element type C3D10) with coefficients C10 = 6.7 KPa and D1 = 0.003 KPa^{-1}, which corresponds to $E = 40$ KPa and $v = 0.49$[12]. The uniaxial tension experiment with an applied strain of 30 % is simulated by applying symmetric tensile displacements along the top and bottom edges. For the compression simulation, the out of plane displacement at the bottom of the substrate is constrained. We first perform buckling analysis to find four Eigen modes. The Eigen modes are then applied as small perturbation to the perfect geometry. Symmetric compressive displacements are applied at two ends, the postbuckling results can be obtained. The option of nonlinear geometry in ABAQUS has been turned on for both tension and compression to account for large deformation. Figure 2l right shows the

maximum principal strain distribution in a local island-serpentine structure. The deformed configurations obtained by FEM match well with the experiment offered in Fig. 2l left. Out-of-plane buckling has been developed in both island and serpentine during compression but just in serpentine during stretching. To compare the mechanical robustness of graphene-hybrid electrode with conventional film electrode mesh, strain distribution in the island after 30 % stretch are presented in Supplementary Fig. 8c. It is clear that graphene-hybrid electrode has relatively smaller strain distribution compared with conventional electrodes. Furthermore, maximum strain as a function of strain is plotted in Fig. 2k, which validates graphene-hybrid electrode experiences lower strains.

1.3.   Selective functionalization using the electrodeposition.

Electrodeposition is an efficient technique for the deposition of functional materials on desired active sites without cross-contaminations. We used PEDOT for the humidity sensor, solid-state Ag/AgCl for the counter electrode, PB with the drop-casted GOx for the glucose sensor, and PANi for the pH sensor, along with the Nafion encapsulation. PEDOT is chosen due to its large impedance change to wetting (Supplementary Fig. 12a bottom). The sweat-uptake of Nafion facilitates the increase of the sensitivity (Supplementary Fig. 3a). The solid-state Ag/AgCl counter electrode enables the sensor operation in the two-electrode system. The solid-state Ag/AgCl electrode exhibits similar OCP values versus commercial Ag/AgCl electrode (Supplementary Fig. 12b bottom). PB is chosen to exploit its high catalytic activity to H_2O_2, which is a by-product of the reaction between GOx and glucose (Supplementary Fig. 12c bottom). PANi is chosen due to its changes of surface protonation at different pH values. After electrodeposition of PANi, the electrode shows larger zeta potential changes at different pH values (Supplementary Fig. 12d bottom). This selective functionalization enables the integration of different types of sensors and counter electrodes on one platform.

1.4.   Effects of environmental conditions on the glucose sensor operation.

Accuracy and sensitivity of the glucose sensor based on glucose oxidase can be affected by environmental conditions such as i) pH, ii) temperature, iii) common drugs, iv) oxygen level, and v) glucose on the skin.

i) pH effect: The pH dependency of the glucose sensor is estimated at different pH values (Supplementary Fig. 14c), and is used to adjust the glucose concentration to obtain corrected glucose concentration (Figs. 3f and 4f).

ii) Temperature effect: The sensitivity of the glucose sensor is slightly decreased as the temperature decreases, while the sensitivity of the pH sensor is similar at various temperatures (Supplementary Fig. 16a,b). The sensitivity variation of the glucose sensor due to the ambient temperature change can be

adjusted by using its pre-calibration data at different temperatures. The ambient temperature can be monitored by the integrated temperature sensor in the diabetes patch.

iii) Interaction with common drugs: The effect of drug interactions on the sensitivity of the glucose sensor is estimated with three commonly used drugs (Tylenol, Aspirin, and Metformin)[13]. We used drug concentrations commonly found in the patient's blood[14,15]. We could selectively measure the glucose concentration without disturbances (Supplementary Fig. 16c). There was a report that Nafion minimized the interference of acetaminophen (Tylenol) in glucose sensing[16]. Our sweat-uptake layer (Nafion) could play a similar role.

iv) Oxygen level effect: Changes of oxygen levels in the blood can affect the sensitivity of glucose sensors based on the glucose oxidase[17-19]. Fluctuations in oxygen concentrations can cause the glucose sensor to underestimate or overestimate glucose levels. However, the glucose oxidase in our glucose sensor is already in contact with the air. The oxygen amount in the air is much larger than that in the blood and/or sweat. The glucose sensor is also calibrated under the air condition. Therefore, the influence on the glucose oxidase would be minimal, although the oxygen concentration in the secreted sweat may be fluctuated. The sweat glucose concentration data measured by our glucose sensor show good linear correlations with those measured by the commercial glucose assay (Supplementary Fig. 17b) and with blood glucose concentration data measured by the commercial glucose meter (Supplementary Fig. 17c).

v) Effect of glucose on the skin: Although there can exist the glucose in the outer layer of skin that is not related with the blood/interstitial fluid/sweat, its amount is not large[20,21] enough to affect the sweat glucose sensing in our diabetes patch. We measured sweat glucose concentrations without considering the glucose in the outer layer of skin and the results showed a good linear correlation with blood glucose concentrations measured by the commercial glucose meter (Supplementary Fig. 17c). The amount of depleted glucose in sweat glucose monitoring process does not disturb the signal read by our diabetes patch. And glucose in stratum corneum[22] which is not related with that in the blood is much lower than sweat glucose levels (0.1~0.7 mM). Therefore, additional warm-up period to ensure the depletion of glucose in the stratum corneum is not needed in our diabetes system.

1.5.   Comparison of the glucose sensor with previous reports.

Our glucose sensor performances are compared with previous reports in references[23-28]. Detection limits, sensing ranges, and sensitivity of each sensor are summarized in Table 3. All glucose sensors including ours show high selectivity by virtue of the glucose oxidase. Although our glucose sensor has comparable performances with previous reports, our diabetes patch can systematically correct potential errors in sweat glucose measurements by pH and temperature fluctuations, providing more accurate

noninvasive sensing than other technologies. Therefore, reliable and repeatable glucose monitoring was available in our diabetes patch.

Table 3. Comparison of state-of-the-art glucose biosensors[23-28].

Base materials	Substrate	Detection limit (μM)	Sensing range (mM)	Sensitivity (μA mM^{-1})	Ref.
GOx/PB/graphene-hybrid	PDMS	10	0.01-0.7	1.0	This work
GOx/Pt NP/graphene	Glass	0.5	0.05-1	580	23
GOx/graphene	Silk	0.1	0.1-10	2.5	24
GOx/Pt NP/graphene petal	Silicon	0.3	0.01-50	0.65	25
GOx/PB	Tattoo	3	0.003-0.1	23	26
GOx/MWCNT/Pt	Glass	20	0.02-1	5.0	27
GOx/MWCNT	GCE	5	0.005-2.5	2.8	28

1.6. Lag time between blood and sweat glucose level.

It is well-known that there is a time lag between blood glucose levels and sweat glucose levels (~20 minutes)[29]. In our 'point-of-care' monitoring system, the humidity sensor first measures relative humidity (RH) changes inside the diabetes patch and then determines the optimum point to start the measurement of other sensors (e.g., glucose and pH sensors). This minimizes detection errors of point-of-care measurements. To maintain the same situation, we started from the sweat collection in every test. On average, it takes ~15 minutes (10~20 minutes) to gather sweat by the sweat-uptake layer in the patch and glucose/pH sensors start to measure when the RH reaches ~80 % (Fig. 4c). Therefore, the sweat glucose concentration data measured by the diabetes patch and the commercial glucose assay are obtained ~15 minutes after the blood glucose concentration data are measured by the commercial glucose meter.

1.7. Feedback therapy using thermo-responsive microneedles.

Bioresorbable polymer microneedles contain drug inside microneedles. Microneedles are immediately dissolved when exposed to fluids, such as the sweat or interstitial fluids. To control the release time and rate instead of instant dissolution/drug release, therefore, we used the PCM, which is spray-coated on microneedles. PCMs, such as fatty acids or fatty alcohols, are biocompatible and/or bio-inert. The PCM used in this study (tridecanoic acid) is thermo-responsive, passivates microneedles, separates microneedles from moistures below the transition temperature, and melts at temperatures above the body temperature (41–42 °C). The HPLC analysis of Metformin concentration *in-vitro* shows that PCM effectively prevents the release of Metformin under the transition temperature of PCM but

allows the drug release above the transition temperature (Fig. 4i and Supplementary Fig. 19b).

Depending on the condition of patients, the amount of drug that needs to be delivered at one time is different. If the patient needs only a small amount of drug at one time, the drug can be delivered in four separate stages as shown in Supplementary Fig. 19d and e. If the patient needs more amount of drug, the amount of drug delivered at one time can be doubled by delivering the drug in two separate stages as shown in Fig. 4j and k. By increasing the total area of microneedles, the maximum number and/or amount of the drug delivery can be increased.

2. References

1) Hrapovic, S., Liu, Y., Male, K. B. & Luong, J. H. T. Electrochemical biosensing platforms using platinum nanoparticles and carbon nanotubes. *Anal. Chem*. **76**, 1083-1088 (2004).

2) Konopka, S. J. & Bruce, M. Diffusion coefficients of ferri- and ferrocyanide ions in aqueous media, using twin-electrode thin-layer electrochemistry. *Anal. Chem*. **42**, 1741-1746 (1970).

3) Anisha, N. P. *et al*. A new view of electrochemistry at highly oriented pyrolytic graphite. *J. Am. Chem. Soc*. **134**, 20117-20130 (2012).

4) Thazhe, V. V., Subbiah, A. & Tharangattu, N. N. The improved electrochemical performance of cross-linked 3D graphene nanoribbon monolith electrodes. *Nanoscale*. **7**, 6504-6509 (2015).

5) Xiaochen, D. *et al*. 3D graphene foam as a monolithic and macroporous carbon electrode for electrochemical sensing. *ACS Appl. Mater. Interfaces*. **4**, 3129-3133 (2012).

6) Guérin, L. J., Bossel, M., Demierre, M., Calmes, S. & Renaud, P. Simple and low cost fabrication of embedded microchannels by using a new thick-film photoplastic. *Proc. Transducers* **2**, 1419-1422 (1997).

7) Williams, J. D. & Wang, W. Using megasonic development of SU-8 to yield ultra-high aspect ratio microstructures with UV lithography. *Microsyst. Technol.* **10**, 694-698 (2004).

8) Kelly, P.F. Properties of Materials. p. 355 (CRC Press, Talyor & Francis Group, 2015).

9) Neerinck, D. G. & Vink, T. J. Depth profiling of thin ITO films by grazing incidence X-ray diffraction. *Thin Solid Films* **278**, 12-17 (1995).

10) Kudin, K. N., Scuseria, G. E. & Yakobson, B. I. C_2F, BN, and C nanoshell elasticity from *ab initio* computations. Phys. Rev. B **64**, 235406 (2001).

11) Wang, A.-J. & McDowell, D. L. In-plane stiffness and yield strength of periodic metal honeycombs. *J. Eng. Mater. Tech.* **126**, 137-156 (2004).

12) Eroshenko, N., Ramachandran, R., Yadavalli, V. K. & Rao, R. R. Effect of substrate stiffness on early human embryonic stem cell differentiation. *J. Biol. Eng*. **7**:7 (2013).

13) Young, D. S., Thomas, D. W., Friedman, R. B. & Pestaner, L. C. *Effects of drugs on clinical laboratory tests*. 4th, **3**, 374-391 (AACC Press, Washington DC, 1995).

14) Tang, Z., Du, X., Louie, F. R. & Kost, J. G. Effects of drugs on glucose measurements with handheld glucose meters and a portable glucose analyzer. *Am. J. Clin. Pathol*. **113**, 75-86 (2000).

15) Hirst, A. J., Farmer, J. A., Ali, R., Roberts, W. N. & Stevens, J. R. Quantifying the effect of metformin treatment and dose on glycemic control. *Diabetes Care*. **35**, 446-454 (2012).

16) Zhang, Y. *et al*. Elimination of the acetaminophen interference in an implantable glucose sensor. *Anal. Chem*. **66**, 1183-1188 (1994).

17) Chun, T.-Y. *et al*. The effect of the partial pressure of oxygen on blood glucose concentration

examined using glucose oxidase with ferricyan ion. *Anesth. Analg.* **79**, 993-997 (1994).

18) Kurahashi, K., Maruta, H., Usuda, Y. & Ohtsuka, M. Influence of blood sample oxygen tension on blood glucose concentration using an enzyme-electrode method. *Crit. Care Med.* **25**, 231-235 (1997).

19) Kost, G. J. *et al.* Multicenter study of oxygen-insensitive handheld glucose point-of-care testing in critical care/hospital/ambulatory patients in the United States and Canada. *Crit. Care Med.* **26**, 581-590 (1998).

20) Kost, J., Mitragotri, S., Gabbay, A. R., Pishko, M & Langer, R. Transdermal monitoring of glucose and other analytes using ultrasound. *Nature Med*. **6**, 347-350 (2000).

21) Xudong, G. *et al*. Detection of trace glucose on the surface of a semipermeable membrane using a fluorescently labeled glucose-binding protein: a promising approach to noninvasive glucose monitoring. *J. Diabetes Sci. Technol*. 7, 4-12 (2013).

22) Takagi, Y., Kriehuber, E., Imokawa, G., Elias, P. M. & Holleran, W. M. β-Glucocerebrosidase activity in mammalian stratum corneum. *J. Lipid Res*. **40**, 861-869 (1999).

23) Zhang, M. *et al.* Highly sensitive glucose sensors based on enzyme-modified whole-graphene solution-gated transistors. *Sci. Rep*. **5**, 8311 (2015).

24) You, X. & Pak, J. J. Graphene-based field effect transistor enzymatic glucose biosensor using silk protein for enzyme immobilization and device substrate. *Sens. Actuators, B* **202**, 1357-1365 (2014).

25) Claussen, J. C. *et al.* Nanostructuring platinum nanoparticles on multilayered graphene petal nanosheets for electrochemical biosensing. *Adv. Funct. Mater.* **22**, 3399-3405 (2012).

26) Bandodkar, A. J. *et al.* Tattoo-based noninvasive glucose monitoring: a proof-of-concept study. *Anal. Chem.* **87**, 394-398 (2015).

27) Tang, H., Yan, F., Lin, P., Xu, J. & Chan, H. L. W. Highly sensitive glucose biosensors based on organic electrochemical transistors using platinum gate electrodes modified with enzyme and nanomaterials. *Adv. Funct. Mater.* **21**, 2264-2272 (2011).

28) Tang, W., Li, L., Wu, L., Gong, J. & Zeng, X. Glucose biosensor based on a glassy carbon electrode modified with polythionine and multiwalled carbon nanotubes. *PLoS ONE* **9**, e95030 (2014).

29) Klonoff, C. D. Noninvasive blood glucose monitoring. Diabetes Care. 20, 433-437 (1997).
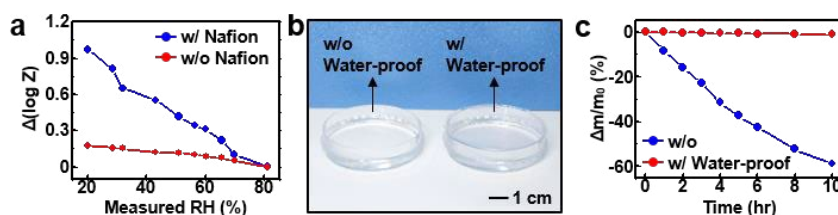
Supplementary Figures
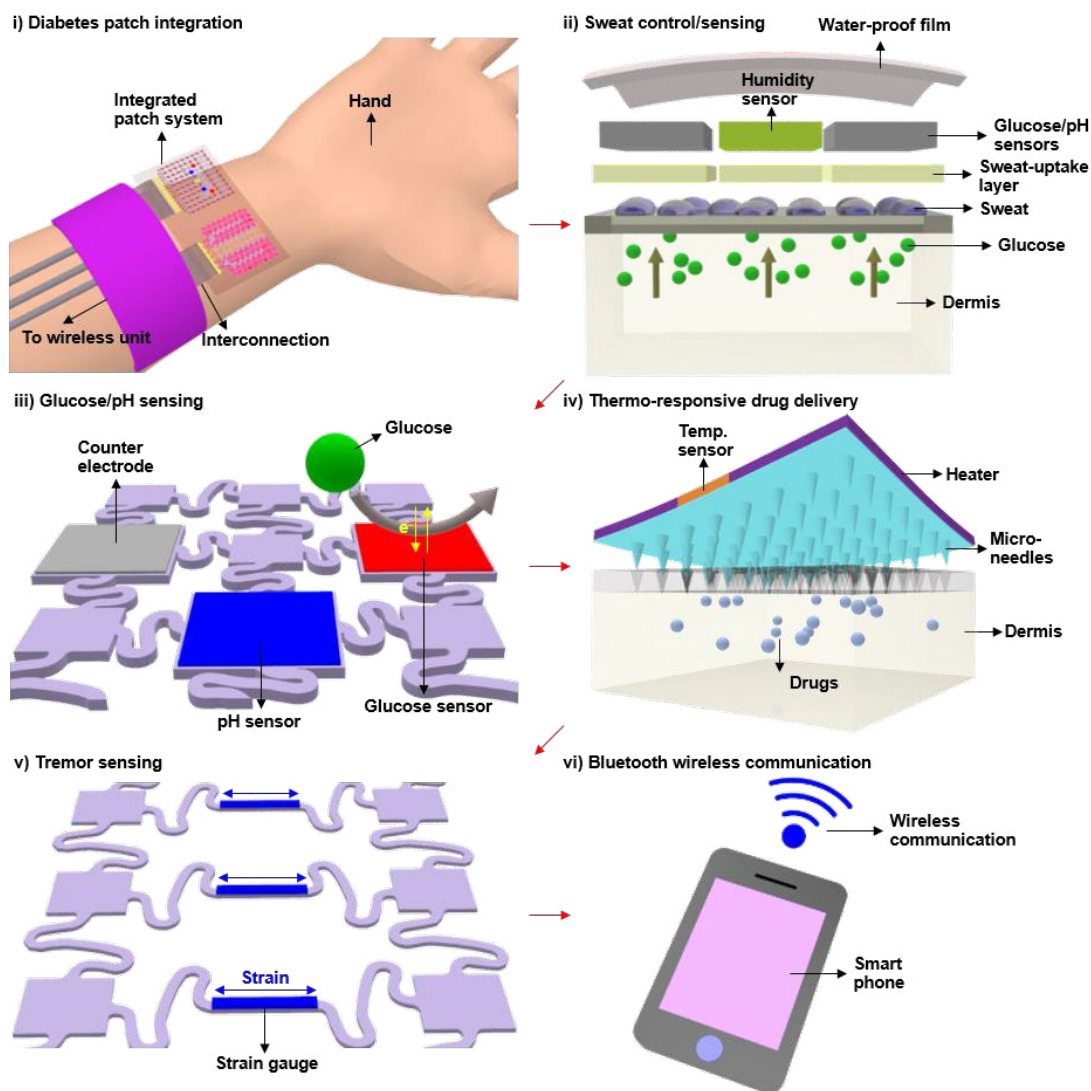
Supplementary Fig. 1. Operation process of the diabetes monitoring and therapy system. Schematic illustrations of the system-level operation. The diabetes patch controls the sweat, in which integrated graphene-hybrid electrochemical sensors monitor markers for diabetes. Thermal actuation through heaters initiates the feedback transdermal drug delivery via thermo-responsive microneedles in the hyperglycaemia. The hypoglycaemia can be detected by the tremor sensor. Monitored data are wirelessly transmitted to remote electronic devices, such as smart phones.
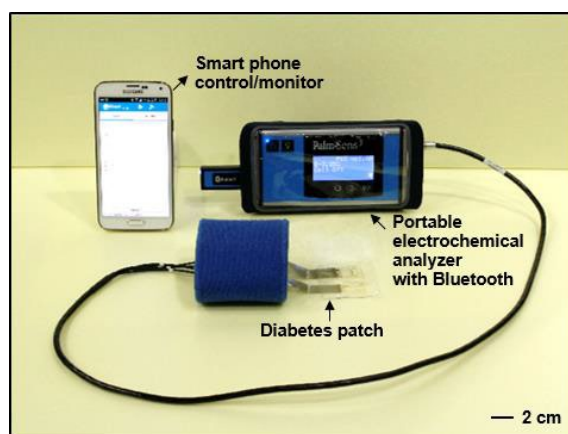
Supplementary Fig. 2. Portable electrochemical analyzer. Graphene-hybrid electrochemical devices are connected to the portable electrochemical analyzer that supplies power to and controls the devices and wirelessly transfers data to remote mobile devices (such as smart phone or tablet computer) via Bluetooth.

Supplementary Fig. 3. Characterization of the sweat-uptake layer and water-proof film. **a,** Characteristic responses of the humidity sensor with (blue) and without (red) the sweat-uptake layer (Nafion). **b,** Optical camera image of the experimental setup for the water evaporation test. The water-proof film is difficult to see due to its transparency. **c,** Relative mass changes of water by the evaporation with (red) and without (blue) the water-proof film.

Supplementary Fig. 4. **Optical images after the PEDOT electrodeposition.** Large scale optical images after the PEDOT electrodeposition on Au film (left), Au mesh (center), and graphene-hybrid electrode (right).
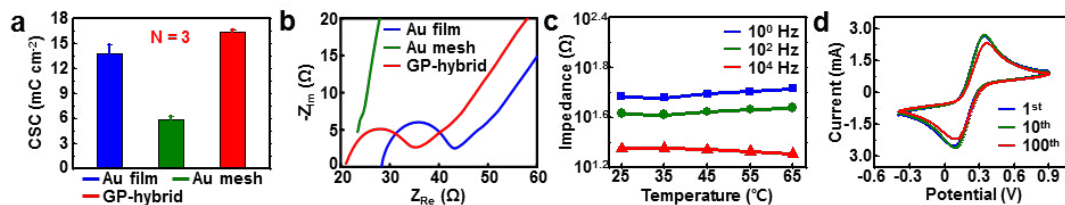
Supplementary Fig. 5. **Electrochemical characterization of graphene-hybrid. a,** Charge storage capacities of the Au film, Au mesh, and graphene-hybrid electrodes in Fig. 2b (number of samples = 3, error bars show the standard deviation). **b,** Magnified view of Nyquist plots of Au film, Au mesh, and graphene-hybrid electrode in PBS with $Fe(CN)_6^{3-/4-}$ at equilibrium potential. **c,** Electrical stability test of graphene-hybrid electrode at different temperatures and AC frequencies in PBS with $Fe(CN)_6^{3-/4-}$ at equilibrium potential. **d,** Stability test of graphene-hybrid electrode after multiple CV measurements in PBS with $Fe(CN)_6^{3-/4-}$ (scan rate: 0.1 V s^{-1} with the commercial Ag/AgCl electrode).
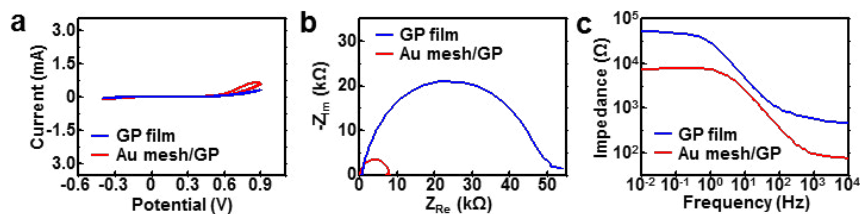
Supplementary Fig. 6. **Electrochemical properties of graphene film and Au mesh/graphene. a,** CV plots of the graphene film and the Au mesh/graphene in PBS with $Fe(CN)_6^{3-/4-}$ (scan rate: 0.1 V s^{-1} with the commercial Ag/AgCl electrode). **b,** Nyquist plots of the graphene film and Au mesh/graphene in PBS with $Fe(CN)_6^{3-/4-}$ at the same potential with that of Fig. 2c. **c,** Bode plots of graphene film and Au mesh/graphene in PBS with $Fe(CN)_6^{3-/4-}$ at the same potential with that of Fig. 2d.
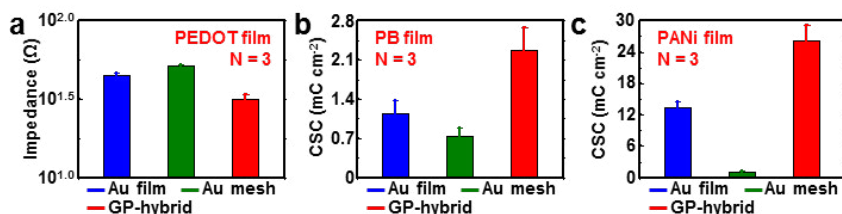
Supplementary Fig. 7. Reproducibility of electrochemical characterization of electrodes (Au film, Au mesh, and graphene-hybrid electrode) after functionalization. a, Impedances of the Au film, Au mesh, and graphene-hybrid electrodes at 100 Hz after electrodeposition of PEDOT under the same condition used in Fig. 2e (number of samples = 3, error bars show the standard deviation). **b,** Charge storage capacities of the Au film, Au mesh, and graphene-hybrid electrodes after electrodeposition of PB under the same condition used in Fig. 2f (number of samples = 3, error bars show the standard deviation). **c,** Charge storage capacities of the Au film, Au mesh, and graphene-hybrid electrodes after electrodeposition of PANi under the same condition used in Fig. 2g (number of samples = 3, error bars show the standard deviation).
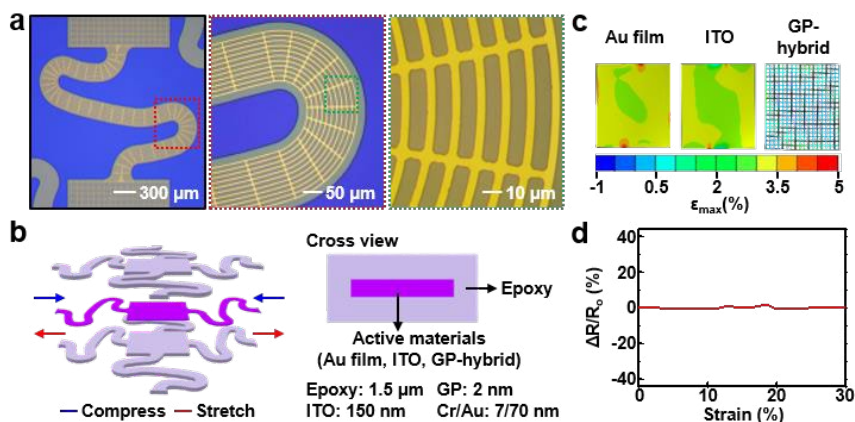
Supplementary Fig. 8. Design strategy and mechanical simulation for the graphene-hybrid electrode. a, Optical microscope images of the Au mesh and graphene bilayer electrode. Serpentine-shaped Au mesh boosts up both the conductivity and mechanical deformability. **b,** Layer information of the graphene-hybrid and conventional electrode. **c,** Strain distribution analysis in the island of Au film, ITO, and graphene-hybrid electrode after 30 % stretching. **d,** Relative resistance change of the graphene-hybrid electrode under applied strains up to ~30 %.
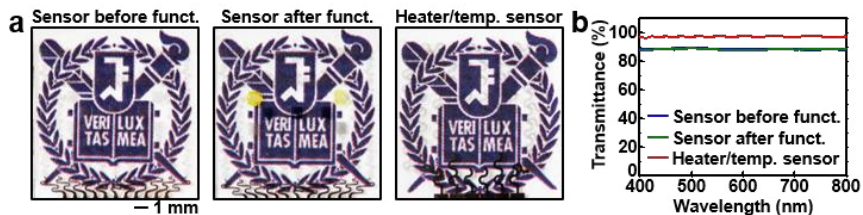
Supplementary Fig. 9. Transparency of the array of graphene-hybrid electrochemical sensors and the heater/temperature sensor. **a,** Optical camera images of the sensor array before (left) and after (center) functionalization on the university logo. Right frame shows the heater/temperature sensor array on the university logo. The logo can be clearly seen through devices due to the transparency. **b,** Corresponding transmittance data of each sample.
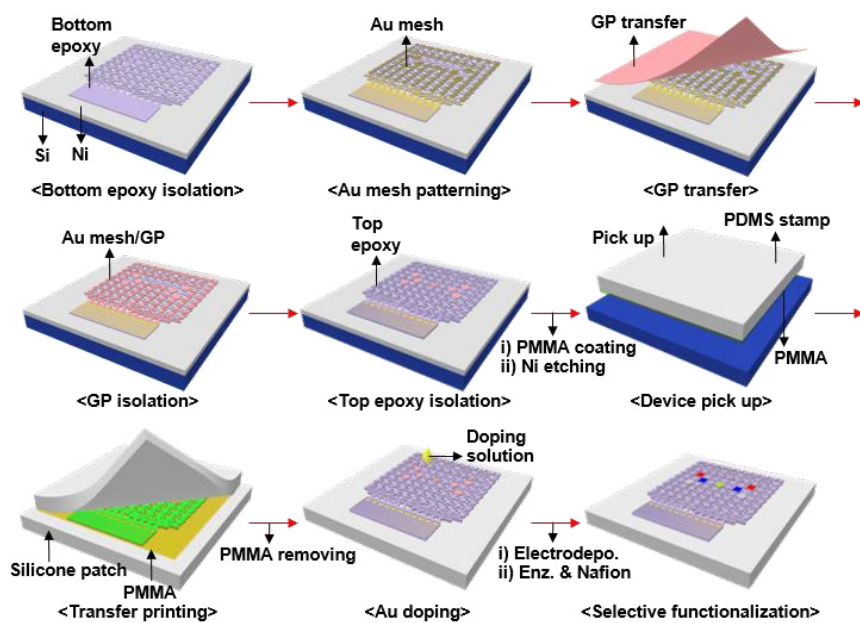
Supplementary Fig. 10. Device fabrication process. Schematic illustration of the fabrication process of the graphene-hybrid electrochemical sensor array.
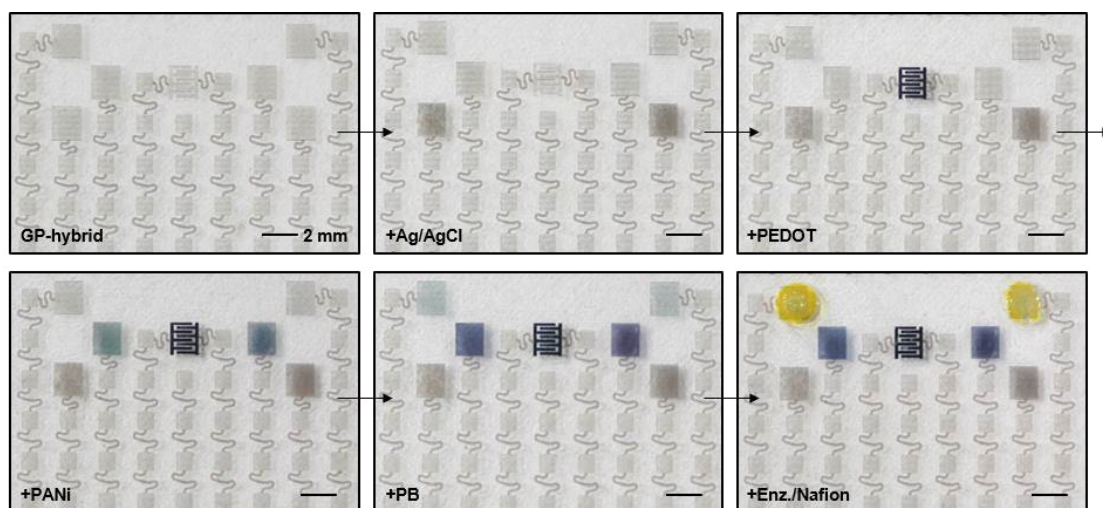
Supplementary Fig. 11. Selective functionalization process of the graphene-hybrid sensors and Ag/AgCl solid-state counter electrode. Optical camera images of the step-wise selective functionalization process of graphene-hybrid. No cross-contaminations are observed.
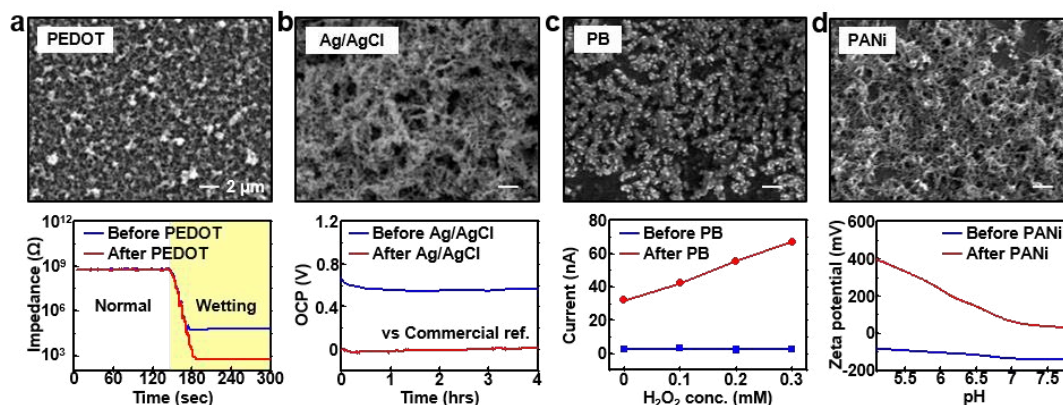
Supplementary Fig. 12. Characterization of functionalized materials of the graphene-hybrid. a, PEDOT electrodeposition on the graphene-hybrid electrode (doped graphene and Au mesh bilayer) for the humidity sensor (top: SEM image, bottom: impedance changes by wetting before and after the PEDOT deposition). **b,** Ag/AgCl electrodeposition for the counter electrode (top: SEM image, bottom: OCP changes before and after Ag/AgCl deposition vs. commercial Ag/AgCl electrode). **c,** PB electrodeposition for the glucose sensor (top: SEM image, bottom: H_2O_2 sensitivity comparison before and after the PB deposition at different H_2O_2 concentrations, initial potential: -0.05 V vs. commercial Ag/AgCl electrode). **d,** PANi electrodeposition for the pH sensor (top: SEM image, bottom: zeta potential changes before and after the PANi deposition).
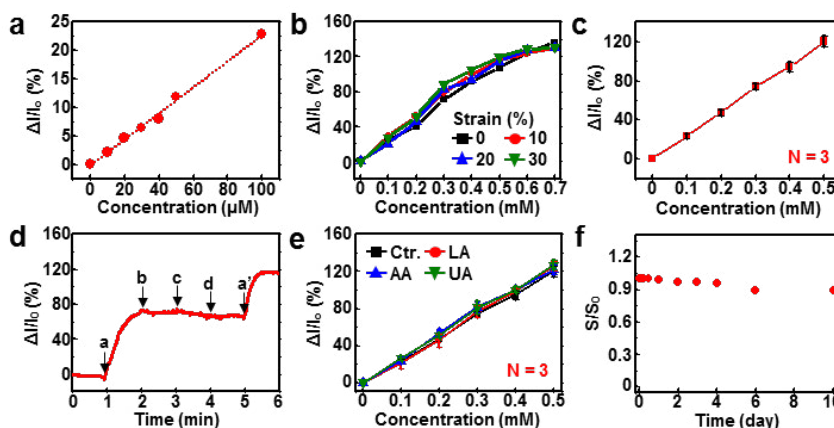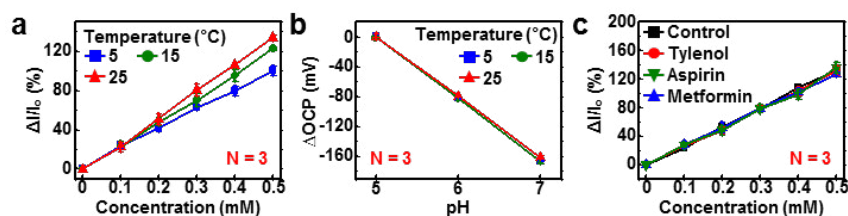
Supplementary Fig. 13. Characterization of glucose sensor. a, Calibration curves of the glucose sensor at low glucose concentrations (initial potential: -0.05 V vs. solid-state Ag/AgCl electrode). **b,** Calibration curves of the glucose sensor at different applied strains (initial potential: -0.05 V vs. solid-state Ag/AgCl electrode). **c,** Reproducible operation of the glucose sensor (number of samples = 3, error bars show the standard deviation, initial potential: -0.05 V vs. solid-state Ag/AgCl electrode). **d,** Selectivity of the glucose sensor (a: 0.3 mM glucose, b: 4 mM lactate, c: 10 μM ascorbic acid, d: 59 μM uric acid, a′: 0.5 mM glucose, initial potential: -0.05 V vs. solid-state Ag/AgCl electrode). Glucose sensor responds to glucose concentration changes only. **e,** Selective operation of the glucose sensor (black: glucose only, red: glucose with 4 mM lactate, blue: glucose with 10 μM ascorbic acid, green: glucose with 59 μM uric acid, number of samples = 3, error bars show the standard deviation, initial potential: -0.05 V vs. solid-state Ag/AgCl electrode). **f,** Long-term stability of the glucose sensor (initial potential: -0.05 V vs. solid-state Ag/AgCl electrode).
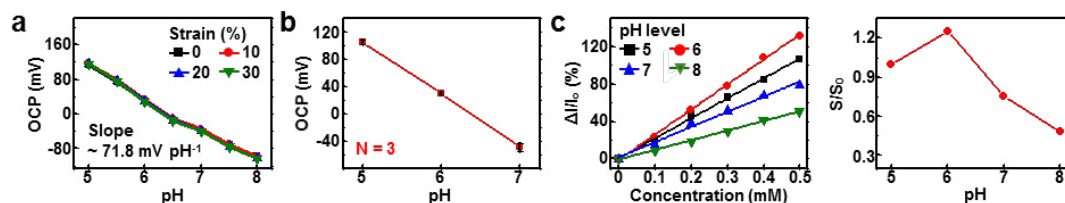
Supplementary Fig. 14. Characterization of pH sensor and pH dependency of glucose sensor. a, pH-dependent OCP changes of the pH sensor at different applied strains (OCP vs. solid-state Ag/AgCl electrode). **b,** Reproducible operation of the pH sensor (number of samples = 3, error bars show the standard deviation, OCP vs. solid-state Ag/AgCl electrode). **c,** pH dependency of the glucose sensor (left: relative current changes of the glucose sensor at different pH, right: relative sensitivity changes of glucose sensor at different pH, initial potential: -0.05 V vs. solid-state Ag/AgCl electrode).
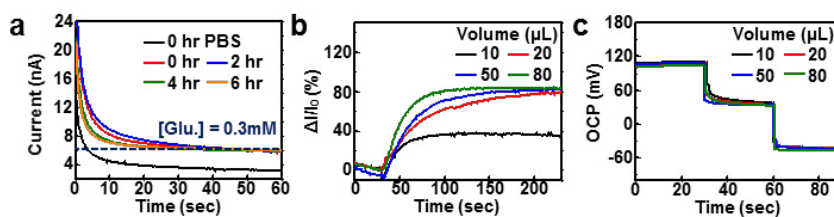
Supplementary Fig. 15. Stability of glucose sensor and influence of sweat amount test on glucose and pH sensors. a, Stability test of the glucose sensor for 6 hours using the artificial sweat (0.3 mM, initial potential: -0.05 V vs. solid-state Ag/AgCl electrode). **b,** Influence of sweat amount (or relative humidity) on the glucose sensor (initial potential: -0.05 V vs. solid-state Ag/AgCl electrode). **c,** Influence of sweat amount (or relative humidity) on the pH sensor (OCP vs. commercial Ag/AgCl electrode).

Supplementary Fig. 16. **Temperature dependency of glucose/pH sensors and drug interaction test of the glucose sensor. a,** Calibration curves of the glucose sensor at different temperatures (number of samples = 3, error bars show the standard deviation, initial potential: -0.05 V vs. solid-state Ag/AgCl electrode). **b,** Open circuit potential changes of the pH sensor at different temperatures (number of samples = 3, error bars show the standard deviation, OCP vs. commercial Ag/AgCl electrode). **c,** Calibration curves of the glucose sensor in a series of test solutions (black: glucose only, red: glucose with 20 µg mL^{-1} Tylenol, green: glucose with 100 µg mL^{-1} Aspirin, blue: glucose with 100 µg mL^{-1} Metformin, number of samples = 3, error bars show the standard deviation, initial potential: -0.05 V vs. solid-state Ag/AgCl electrode).
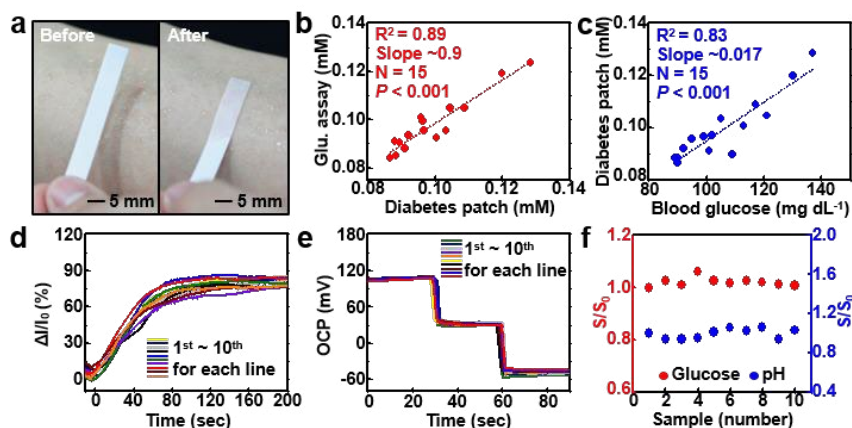
Supplementary Fig. 17. Sweat generation, statistical correlation, and multiple reuses. a, Optical camera images of the generated sweat, checked by the cobalt chloride paper. **b,** Statistical analysis of the correlation between the sweat glucose concentration measured by the diabetes patch and that measured by the commercial glucose assay. Small P value shows that the results are statistically reliable ($P < 0.001$). **c,** Statistical analysis of the correlation between the sweat glucose concentration measured by the diabetes patch and the blood glucose concentration measured by the commercial glucose meter. Small P value shows that the results are statistically reliable ($P < 0.001$). **d,** Stable operation of the glucose sensor after multiple reuses (initial potential: -0.05 V vs. solid-state Ag/AgCl electrode) using the artificial sweat (0.3 mM). **e,** Stable operation of the pH sensor after multiple reuses (OCP vs. solid-state Ag/AgCl electrode) using standard pH buffer solutions (pH 5, 6, 7). **f.** Plots showing the stable sensitivity of glucose and pH sensor in multiple sensors.
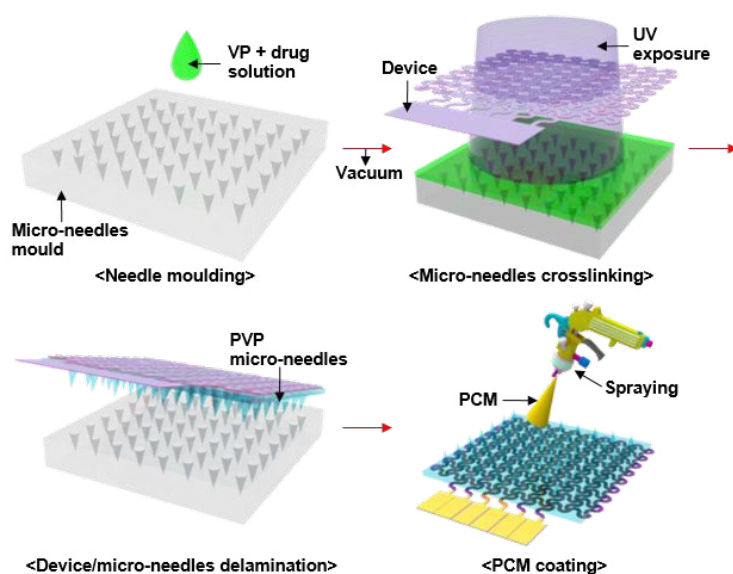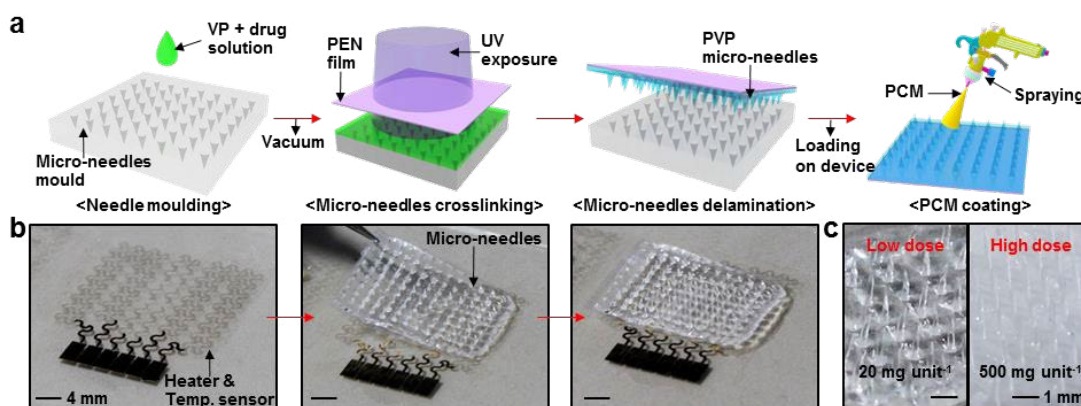
Supplementary Fig. 18. Fabrication process of the drug-loaded microneedles. Schematic illustrations of the fabrication process of the drug-loaded microneedles. Microneedles are made of the bioresorbable polymer (PVP) and coated with the biocompatible PCM (tridecanoic acid).
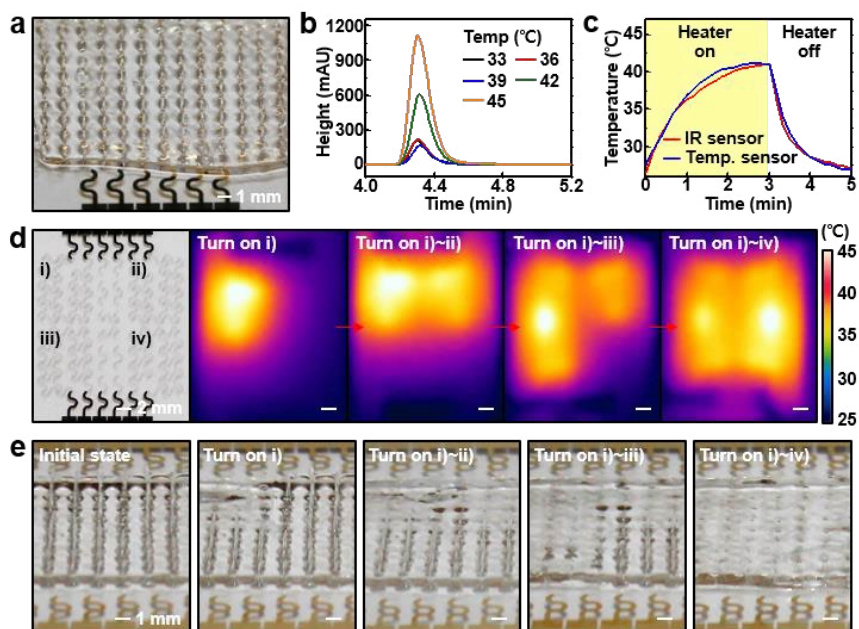
Supplementary Fig. 19. **Characterization of microneedles, embedded heaters, and a temperature sensor. a,** Optical camera image of microneedles integrated on the array of heaters and a temperature sensor. **b,** HPLC analysis data of drug concentrations during the thermo-responsive drug release of Fig. 4i. **c,** Temperature monitoring of the heater by using a commercial infrared camera and the integrated temperature sensor. **d,** Step-wise thermal actuation of microneedles by using the 4 channel heater array. This enables the multi-step drug release. **e,** Optical camera images of the step-wise dissolution of microneedles corresponding to the thermal actuation in Supplementary Fig. 19d.
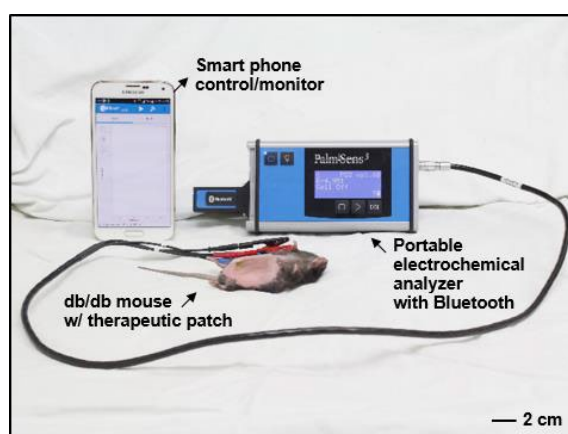
Supplementary Fig. 20. *In vivo* **animal experiment setup for the transdermal drug delivery using thermo-responsive microneedles.** Image of the *in vivo* experimental setup for the integrated therapeutic system (drug-loaded microneedles, heater, and a temperature sensor) connected to the portable electrochemical analyzer.

Supplementary Fig. 21. Fabrication process and images of the replacement type microneedles. a, Schematic illustrations of the fabrication process of the drug-loaded microneedles. **b,** Optical image of replacement type microneedles on the heater and temperature sensor (left: before transfer, middle: during transfer, right: after transfer). **c,** Optical images of replacement type microneedles with different amount of loaded Metformin (left: low dose; ~20 mg unit^{-1}, right: high dose; ~500 mg unit^{-1}).